Proceedings of the 6th IFAC Symposium on Mechatronic Systems, Zhejiang University, Hangzhou, China, April 10-12, 2013

IFAC MECH2013-0086

Kinematic Design and Analysis of a 6-DOF Upper Limb Exoskeleton Model for a Brain-Machine Interface Study ⋆

Junkai Lu *, **Wenjie Chen** *, and **Masayoshi Tomizuka** *

* *Department of Mechanical Engineering, University of California, Berkeley, CA 94720 USA (e-mail: {junkai.lu, wjchen, tomizuka} @berkeley.edu).*

Abstract: The integration of the brain-machine interface (BMI) and the exoskeleton technique has the potential to promote the understanding of fundamental principles in neural control of movement, as well as to motivate a new generation of rehabilitation or power augmentation exoskeleton systems. In this paper, the kinematic design and development of a 6-DOF upper limb exoskeleton for a BMI study is presented. In order to achieve a singularity-free design of the shoulder complex, a 4-DOF shoulder complex model is proposed using one redundant DOF in contrast to the commonly used orthogonal triad model. The feasibility of both singularity and joint limit avoidance control is investigated based on the reachability analysis.

Keywords: upper limb exoskeleton, kinematic singularity, reachability analysis, kinematic control, brain-machine interface

1. INTRODUCTION

Paralysis caused by damage to the nervous system affects about 5.6 million people in the U.S. (Christopher & Dana Reeve Foundation, 2009) by eliminating or weakening control of parts of the body. Loss or difficulty of upper-limb mobility is one of its major effects. Since the introduction of the brain-machine interface (BMI), a direct pathway enabling communication between the brain and an external apparatus, researchers have been putting tremendous efforts into finding ways to enable paralyzed people to move a prosthetic device with their mind. In upper extremity rehabilitation, most of the existing therapy robots are either end-effector-based or exoskeleton devices (Nef and Riener, 2008). Since end-effector-based robots generally interact with patients only through one point (the end-effector), it fails in fully determining the arm postures and the interaction torques of each joint. The wearable exoskeleton, in spite of more complicated mechanical structure and system dynamics, has multiple contact points with the body, allowing both applying control to and getting feedback from each joint. The integration of BMI study and exoskeleton technique is a promising direction of future prosthetic devices. This innovation has the potential to promote human's understanding of fundamental principles in the neural control of movement in scenarios involving physical interactions with the world, as well as to motivate new generation of rehabilitation or power augmentation exoskeleton systems.

This paper presents the development of a 6-DOF passive exoskeleton design for the joint motion data acquisition from a BMI macaque. It shares the common design difficulties with those designed for humans. Apart from the

hand, the anatomy of the shoulder complex is the most difficult part to model for an upper limb exoskeleton. The shoulder complex consists of four joints that function in a precise and coordinated manner: the sternoclavicular (SC) joint, the acromioclavicular (AC) joint, the glenohumeral (GH) joint, and the scapulothoracic (ST) joint (Peat, 1986). The GH joint is the main joint of the shoulder and is usually referred to as the shoulder joint. It has three degrees of freedom (DOF), and is commonly described by a "ball-and-socket" model. Three revolute joints are used in Johnson et al. (2001); Tsagarakis and Caldwell (2003); Martinez et al. (2008) to model the GH joint. This orthogonal triad model (denoted as "GH3-I"), however, has an inherent singularity problem when the first and the third axes align with one another. To reduce the occurrence of singularities, some researchers chose to put the singularities out of the prescribed workspace by optimizing the relative angles between the three axes (Ball et al., 2007; Letier et al., 2008) (denoted as "GH3-II"), or in the directions that are anthropometrically hard to reach (Perry et al., 2007) (denoted as "GH3-III"). In order to solve the singular problem arising with the inherent singular nature of an orthogonal triad, a 4-DOF GH model (denoted as "GH4") is proposed in this paper. By introducing an extra DOF, the system complexity is increased. A kinematically redundant mechanism, however, has more flexibility for positioning and trajectory tracking due to its possession of more DOFs than required.

The reason why the singularity issue is of great concern is that the proposed exoskeleton will be used by macaques, which are much less cooperative than humans. During the BMI manual control, the macaque is assumed to be able to move freely in its range of motion (ROM) with the exoskeleton passively collecting the motion data. Both the

macaque's safety and its ROM should be guaranteed by avoiding the singularities in the whole workspace.

The exoskeleton design presented in this paper is a non-motorized prototype to verify the feasibility of the proposed upper limb model. The proposed modeling and mechanical design are described in Section 2 based on the discussion on the upper limb model and the design requirements. Kinematic analysis of the proposed 4-DOF shoulder complex model is conducted in Section 3 in terms of the model's joint limits, singularity, and manipulability. The feasibility of implementing singularity and joint limit avoidance control for the actuated version of this model is analyzed in Section 4 based on the backward reachability study. The conclusion is given in Section 5.

2. SYSTEM DESIGN

2.1 Upper Limb Model

The functionality of the primate upper limb is determined by the shoulder complex, elbow, wrist, and the hand, performing multiple integrated spheres of action (Bowker, 1992). The shoulder complex is a highly-coupled mechanism of great complexity due to its possession of 3 DOFs in each of the SC, AC, GH, and ST joints. A 5-DOF mathematical model of the shoulder complex is introduced in Yang et al. (2005), including three rotational DOFs and two translational DOFs, with the thorax as the fixed base.

In order to simplify the system modeling and design in the engineering world, mostly the GH joint is modeled for the shoulder complex as a ball-and-socket joint model which consists of three rotational DOFs, as shown in Fig. 1(a). Two conventions of describing the rotation sequence are mainly adopted in the biomechanics community, and they both work in the way of using a triad with two orthogonal axis pairs to represent the GH joint. Fig. 2(a) shows a most commonly used convention of "flexion-abduction-rotation" (denoted as "Convention A") inherited from the clinical terms and thus has the functional anatomical meaning. The convention of "azimuth-elevation-roll" (denoted as "Convention B") depicted in Fig. 2(b) is more of a mathematical way of describing spherical coordinates. Since azimuthal rotation occurs with respect to a fixed vertical axis and elevation/depression takes place about the horizontal plane, this coordinate definition is easier to visualize (Romilly et al., 1994). Some research groups have also taken two translational DOFs into consideration. Mihelj et al. (2007) added one extra prismatic joint to assist shoulder elevation/depression, and Ball et al. (2007) managed to include both shoulder elevation/depression and protraction/retraction at the cost of more system complexity.

The elbow joint is commonly modeled using a single-axis hinge joint as shown in Fig. 1(b). The effect of the angular variations between the hinge joint axis and the forearm pronosupination axis during full elbow flexion and full extension is also discussed in Perry et al. (2007). Although the inclusion of an oblique angle from the elbow flexion-extension axis to both the upper and the lower arm segments can account for a more accurate elbow model, a perpendicular relation with no hinge offset is usually utilized for simplicity.
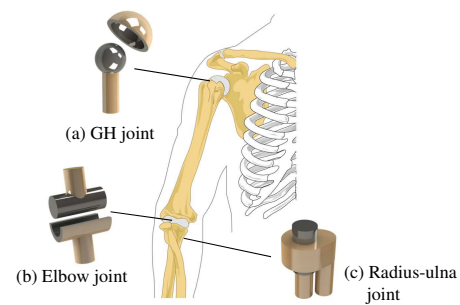

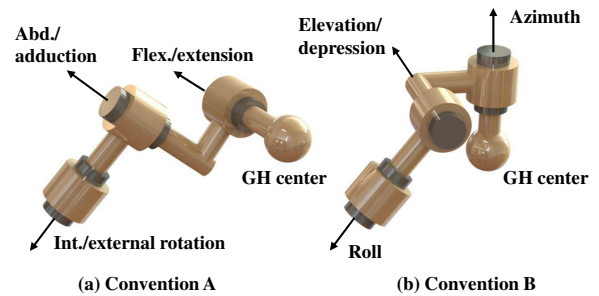Fig. 1. Mechanical models of the upper limb joints.

Fig. 2. Two rotation conventions for GH joint model.

Fig. 1(c) shows a pivot joint representation of the radioulnar articulation corresponding to pronosupination of the forearm. This DOF can be included either to the elbow or to the wrist.

In our BMI study it is assumed that the macaque is allowed to freely use its hand to grasp targets without the exoskeleton components on the wrist or the hand. Thus wrist and hand motions and their modeling are not investigated in this paper.

2.2 Design Requirements

Compared with an exoskeleton designed for humans, a compact design is of more importance for an exoskeleton to be worn by the macaques due to their relatively small body sizes. Since the ROM of macaques is not available in existing literatures, human's ROM for activities of daily living (ADL) is referenced when designing the exoskeleton's mechanical limits. Human's maximum physiological ROM and ADL ROM are respectively listed in the third and the fourth columns of Table 1 (averaged from Cott and Kinkade (1972); Perry et al. (2007); Ergin and Patoglu (2012)), and are assumed to be sufficient to cover the ROM of macaques. Besides, it is assumed that the shoulder elevation/depression and protraction/retraction of the macaques are not evident during their upper limb movement. Thus for simplicity, these two translational DOFs of the shoulder complex are not considered here.

In terms of manipulability of the mechanism, a singularity-free design is desired to both maximize the macaques' workspace and guarantee their safety. Although the safety issue is not involved in a fully passive mechanism, it will be a great concern for the future motorized exoskeleton design. The manipulability and singularity will be further discussed in Section 3.

Table 1. Human's ROM and the designed mechanical limits.

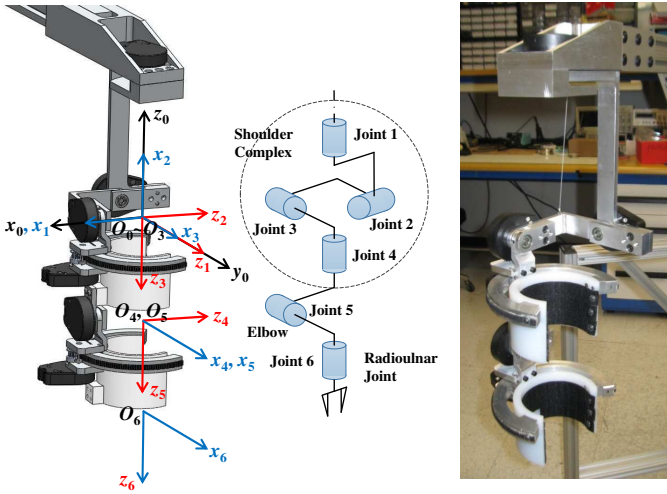| Joint	Motion	Phy. ROM	ADL ROM	Mech. Limit
1	azi. add.	–	140°	140.5°
	azi. abd.	–	30°	50.5°
2	shld. add.	134°	130°	138.3°
	shld. abd.	48°	15°	138.3°
3	shld. flx.	188°	80°	188.1°
	shld. ext.	61°	30°	8.1°
4	shld. int.	97°	70°	80.0°
	shld. ext.	90°	80°	80.0°
5	elbw. flx.	142°	140°	88.7°
	elbw. ext.	0°	0°	8.1°
6	pron.	77°	65°	80.0°
	supi.	113°	70°	80.0°

Fig. 3. Left: CAD model with coordinate frames. Middle: Simplified joint model. Right: Physical hardware design implementation.

2.3 Mechanical Design

Here we propose a 6-DOF model of the macaque's upper limb with each DOF represented by a single-axis revolute joint as shown in Fig. 3. Four DOFs are assigned to the shoulder complex with Joint 1 corresponding to azimuthal rotation, Joint 2 abduction/adduction, Joint 3 flexion/extension, and Joint 4 internal/external rotation. These four revolute joints together form a spherical joint model of the shoulder complex intersecting at a point representing the center of the GH joint. The elbow joint and the radioulnar joint are each modeled by one DOF labeled as Joint 5 and Joint 6, respectively.

The prosthetic joints of this wearable upper limb exoskeleton can be classified into two types: rotation axis being perpendicular to the arm segments (Type I), and rotation axis being along the longitude of the arm segments (Type II). In our proposed design (Fig. 3), Joint 1, 2, 3, and 5 are of Type I. Fig. 4(a) shows the design example of Joint 2. Joint 4 and 6 are of Type II (Fig. 4(b)), and designs involving a curved guide rail are most commonly used to construct this mechanism (Mihelj et al., 2006; Perry et al., 2007). In our design, Joint 4 and Joint 6 utilize the same mechanism. A cuff with 1/3 circle opening is used for the macaques to put on. A curved guide rail with a timing belt and a sliding roller with the corresponding pulley are
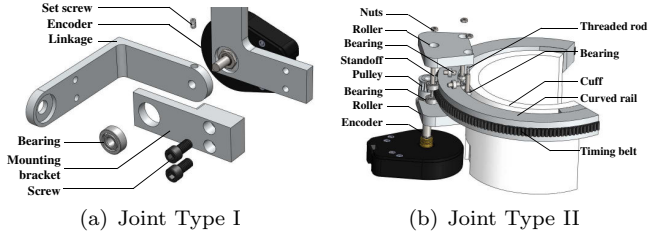

(a) Joint Type I   (b) Joint Type II

Fig. 4. CAD design of two types of joints.

mounted on the cuff to transmit the upper/lower arm's rotation movement to the sensors. Two commercial braces are used to firmly attach the arm to the cuff with Velcro.

The designed mechanical limits for these six joints are listed in the last column of Table 1. Compared with the human ADL ROM, most of the mechanical joint limits meet the design requirements. In fact, in our BMI study, the macaque's working space is prescribed as always in front of its coronal plane and the macaque's task does not involve elbow flexion of over 90°. Thus, the designed shoulder extension and the elbow flexion limits are sufficient even though they are smaller than those of ADL ROM. In other words, this proposed design can cover most of the human's ROM, which is much more than required for the macaque's workspace in this BMI study.

3. KINEMATIC ANALYSIS

3.1 System Kinematic Model

Forward Kinematics   Forward kinematics defines the subject's wrist position and orientation in the base frame as a function of the joint variables. The wrist position vector $\boldsymbol{p}^0$ and the orientation vectors $(\boldsymbol{n}^0, \boldsymbol{s}^0, \boldsymbol{a}^0)$ can be obtained by calculating the coordinate transformation matrix $\boldsymbol{T}_6^0(\boldsymbol{\theta})$ describing the wrist Frame 6 with respect to the base Frame 0

$$\boldsymbol{T}_6^0(\boldsymbol{\theta}) = \boldsymbol{A}_1^0 \boldsymbol{A}_2^1 \boldsymbol{A}_3^2 \boldsymbol{A}_4^3 \boldsymbol{A}_5^4 \boldsymbol{A}_6^5 = \begin{bmatrix} \boldsymbol{n}^0 & \boldsymbol{s}^0 & \boldsymbol{a}^0 & \boldsymbol{p}^0 \\ 0 & 0 & 0 & 1 \end{bmatrix} \quad (1)$$

where $\boldsymbol{\theta} = [\,\theta_1 \; \theta_2 \; \theta_3 \; \theta_4 \; \theta_5 \; \theta_6\,]^{\mathrm{T}}$ denotes the joint space angles, and $\boldsymbol{A}_i^{i-1}$ is the transformation matrix from Frame i to Frame $i-1$. The frame definition shown in Fig. 3 follows the Denavit-Hartenberg (DH) parameter convention.

Jacobian Matrix   A linear mapping between the task space velocity $\boldsymbol{v}_e$ and the joint space velocity $\dot{\boldsymbol{\theta}}$ can be established via the Jacobian matrix as

$$\boldsymbol{v}_e = \boldsymbol{J}(\boldsymbol{\theta})\dot{\boldsymbol{\theta}} \quad (2)$$

where $\boldsymbol{v}_e = [\,\dot{\boldsymbol{p}}_e^{\mathrm{T}} \; \boldsymbol{\omega}_e^{\mathrm{T}}\,]^{\mathrm{T}}$ and $\boldsymbol{J}(\boldsymbol{\theta}) = [\,\boldsymbol{J}_p(\boldsymbol{\theta})^{\mathrm{T}} \; \boldsymbol{J}_o(\boldsymbol{\theta})^{\mathrm{T}}\,]^{\mathrm{T}}$. The end point linear velocity $\dot{\boldsymbol{p}}_e$ and the angular velocity $\boldsymbol{\omega}_e$ can be then expressed as

$$\dot{\boldsymbol{p}}_e = \boldsymbol{J}_p(\boldsymbol{\theta})\dot{\boldsymbol{\theta}}, \quad \boldsymbol{\omega}_e = \boldsymbol{J}_o(\boldsymbol{\theta})\dot{\boldsymbol{\theta}} \quad (3)$$

3.2 Workspace and Joint Limits

Workspace is the region described by the origin of the end-effector frame when all the joints execute all possible motions (Siciliano et al., 2009). The workspace of the proposed 6-DOF upper limb exoskeleton is fully determined by the mechanical limits listed in Table 1. For a motorized

device, the joint limits need to be avoided to guarantee system's performance.

3.3 Singularity Analysis

The Jacobian matrix is a function of the joint space configuration $\boldsymbol{\theta}$, and those configurations at which $\boldsymbol{J}(\boldsymbol{\theta})$ is rank-deficient are termed *kinematic singularities* (Siciliano et al., 2009). For any mechanism that uses a series of revolute joints to mimic the ball-and-socket joint, singularities always exist. When singularity occurs, at least one DOF of rotation is lost, and the mechanism cannot move arbitrarily, which is highly undesirable for a motion tracking system. Meanwhile, in the vicinity of a singularity for a motorized design, small desired velocities in the task space will require very large joint motions if the task space velocities have components along the degenerated directions. These large joint motions may damage the motors or even result in severe harm to the subjects. Thus the singularity issue is emphasized here. Since the designs of the elbow joint and the forearm rotation joint are following the subject's anatomical structure, the subject's natural actuation DOFs should be preserved at these two joints. Thus, we are only interested in the motion realization by the other four joints (the shoulder complex model), in particular, the singularity and joint limits avoidance of these four joints. For this spherical shoulder complex model with fixed upper arm length, the end point is moving on a spherical surface. Thus the orientation Jacobian $\boldsymbol{J}_o(\boldsymbol{\theta})$ [1] will be investigated, and can be expressed as

$$\boldsymbol{J}_o(\boldsymbol{\theta}) = \begin{bmatrix} 0 & -s_1 & c_1 s_2 & -c_1 c_2 s_3 - s_1 c_3 \\ 0 & c_1 & s_1 s_2 & -s_1 c_2 s_3 + c_1 c_3 \\ 1 & 0 & c_2 & s_2 s_3 \end{bmatrix} \quad (4)$$

where $s_i = \sin(\theta_i)$, and $c_i = \cos(\theta_i)$.

Using (4) we can find that the orientation Jacobian matrix $\boldsymbol{J}_o(\boldsymbol{\theta})$ will lose rank (i.e., singularity will occur) for the following four cases:

(1) $\theta_2 = -\pi$, $\theta_3 = 0$, θ_1 and θ_4 are arbitrary;
(2) $\theta_2 = -\pi$, $\theta_3 = \pi$, θ_1 and θ_4 are arbitrary;
(3) $\theta_2 = 0$, $\theta_3 = 0$, θ_1 and θ_4 are arbitrary;
(4) $\theta_2 = 0$, $\theta_3 = \pi$, θ_1 and θ_4 are arbitrary.

Note that not all of these four configurations are the actual singularities of this 4-DOF shoulder complex model. The ranges of the first four joint angles [2] are listed in Table 2 based on the mechanical limits and the ADL ROM illustrated in Table 1. Thus among the aforementioned four potential singularities, there is only one singular configuration within the defined joint angle ranges, i.e., when $\theta_2 = -\pi$ and $\theta_3 = 0$, corresponding to the situation where Joint 1 is collinear with Joint 3, and Joint 2 is collinear with Joint 4, respectively, as shown later in Fig. 7.

---

[1] Hereafter, $\boldsymbol{\theta} = [\,\theta_1 \ \theta_2 \ \theta_3 \ \theta_4\,]^{\mathrm{T}}$ and $\boldsymbol{J}_o(\boldsymbol{\theta}) \in \mathbb{R}^{3 \times 4}$ due to the emphasis on the 4-DOF shoulder complex model.
[2] Note, angles in Table 1 are defined in the way commonly used in the biomechanics world, while angles in Table 2 are defined following the DH parameter convention in Fig. 3, with home position of $\theta_1 = 0$, $\theta_2 = -\pi/2$, $\theta_3 = \pi/2$, and $\theta_4 = 0$.

Table 2. Ranges of the joint space angles.

Angle	θ_1	θ_2	θ_3	θ_4
Range (°)	$-50 \sim 140$	$-228 \sim -60$	$-98 \sim 98$	$-80 \sim 80$

3.4 Manipulability Analysis

Compared with the commonly used 3-DOF shoulder complex model, this proposed 4-DOF mechanism has the advantage of always being able to avoid its singular configuration by appropriately planning the trajectory with the one redundant DOF. In order to quantitatively measure the manipulating capability of the mechanism to arbitrarily change its position and orientation, the concept *manipulability* is proposed by Yoshikawa (1985) as

$$c_m(\boldsymbol{\theta}) = \sqrt{\det(\boldsymbol{J}(\boldsymbol{\theta})\boldsymbol{J}(\boldsymbol{\theta})^{\mathrm{T}})} \quad (5)$$

and $c_m(\boldsymbol{\theta})$ vanishes at the singular configurations.

In general, the manipulability of a mechanism is dependant on its scale, number of joints, and the dimension of its task space. In order to compare manipulabilities of different manipulators working in different workspaces, Kim and Khosla (1991) proposed the concept *relative manipulability* which is independent of scales and dimension orders:

$$c_{rel}(\boldsymbol{\theta}) = \frac{\sqrt[m]{\det(\boldsymbol{J}(\boldsymbol{\theta})\boldsymbol{J}(\boldsymbol{\theta})^{\mathrm{T}})}}{\sqrt{\sum\limits_{i=1}^{n} (a_i^2 + d_i^2)}} \quad (6)$$

where n is the number of the joints, m is the dimension order of the task space, and a_i and d_i are the i-th link length and the i-th joint offset defined in the DH parameter convention, respectively.

As an example to demonstrate the advantage of the proposed design, the manipulability distributions of the rotational degrees of freedom on the task space horizontal plane (i.e., the $x_0 O_0 y_0$ plane defined in Fig. 3) are investigated for the following four models: the orthogonal triad model "GH3-I" (IKO, Martinez et al. (2008)), the triad models with rarely-reached singular direction "GH3-II" ((CADEN)-7, Perry et al. (2007)), and with optimized relative angles "GH3-III" (MEDARM, Ball et al. (2007)), as well as our proposed "GH4" model. By setting the upper arm segment as unit length, the denominator in (6) equals to 1 for all of the four models regardless of the joint number n. Besides, in this study, the task space dimension order is the same (i.e., 3) for all four models and thus the manipulabilities are comparable as long as we use the same m for each model. Here we set $m = 2$ so as to be consistent with the commonly used measure defined in (5). Therefore, the manipulability of our GH4 model can be expressed as

$$c_{m,GH4}(\boldsymbol{\theta}) = \sqrt{\det(\boldsymbol{J}_o(\boldsymbol{\theta})\boldsymbol{J}_o(\boldsymbol{\theta})^{\mathrm{T}})}$$
$$= \sqrt{s_2^2 + s_3^2 + s_2^2 c_3^2 + c_2^2 s_3^2} \quad (7)$$

Fig. 5 plots the manipulability distributions of the four models, and the color of the end point on the trajectory represents the manipulability value at that particular posture. For "GH3-III" and "GH4" in which the inverse kinematic solutions are not unique, only the maximum manipulability values of each end point on the horizontal plane are plotted.

(a) GH3-I (IKO) model

(b) GH3-II ((CADEN)-7) model

(c) GH3-III (MEDARM) model
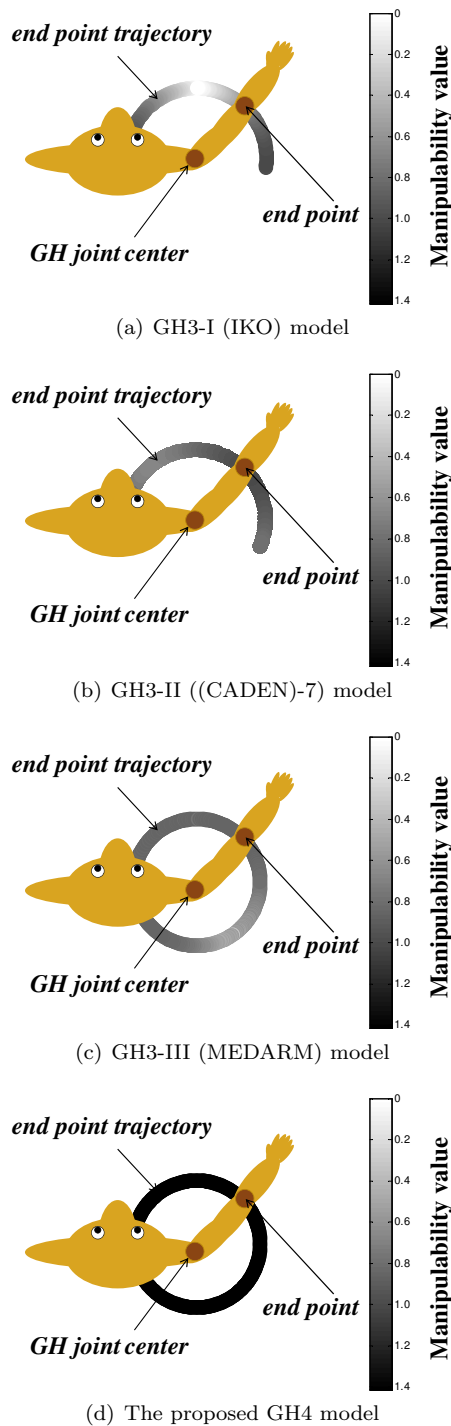

(d) The proposed GH4 model

Fig. 5. Manipulability distributions of four models on the horizontal plane. (Macaque is plotted with its GH joint center fixed and its elbow as the end point.)

Fig. 5(a) shows the manipulability plot of the GH3-I model (IKO). It uses rotation Convention A with the strict forward direction as its singular direction on the horizontal plane. Each posture is uniquely determined by one joint space realization due to its possession of only three DOFs, which means singularities will always occur in the vicinity of the strict forward direction and one rotational DOF (either shoulder flexion/extension, or abduction/adduction) will be lost.

Fig. 5(b) presents the manipulability distribution of the GH3-II model ((CADEN)-7). This design is also an orthogonal triad model using the rotation Convention A. But with the first joint axis having an acute angle about the vertical direction, the singularity of this model was designed in a direction that is rarely (statistically) reached by the subject. Thus compared with GH3-I, there is no "hard" singularities within the feasible workspace (in the horizontal plane), and the average manipulability is improved. However, singularities still exist in some other regions of the workspace (outside the horizontal plane). Therefore, it is still possible for the subject to enter the vicinity of the singular region, resulting in limited feasible workspace.

Fig. 5(c) plots the manipulability distribution of the GH3-III model (MEDARM). It features the first two revolute axes with an optimized angle rather than an orthogonal relationship. By inclusion of an "azimuth" (not a full azimuth) axis, the ROM on the horizontal plane is extended, though some regions are physically unable to reach for a macaque. Besides, the not unique inverse kinematic solutions lead to multiple joint space realizations (in each direction on this plane). Thus it has more flexibility regarding the upper arm's motion on the horizontal plane. However, its average manipulability is relatively low due to its lack of a dedicated internal/external rotation joint for the upper arm.

Fig. 5(d) shows the manipulability distribution of our proposed model with four DOFs combining both of the two GH joint rotation conventions (Convention A and B). From Fig. 5(a) to Fig. 5(d), the improvement of the manipulabilities is evident. With an azimuth axis, this model enjoys the similar multiple joint space realizations as the MEDARM model on the horizontal plane. The inclusion of a standard triad model (GH3-I) following the azimuthal DOF makes it possible to obtain the maximal manipulability value ($\sqrt{2}$) in all directions (i.e., the feasible workspace is the whole horizontal plane). In fact, each posture of the proposed GH4 model possesses different levels of manipulabilities, and thus it is possible to avoid the singular configuration by properly selecting the trajectories.

4. FEASIBILITY OF SINGULARITY AND JOINT LIMITS AVOIDANCE

Our ultimate goal is to design an actuated upper limb exoskeleton with several control modes, to realize both passive data acquisition and active control of the macaque's upper limb motion for the BMI study. This actuated exoskeleton may follow the structure of the current passive version. Thus it is of interest to verify whether the designed exoskeleton structure is able to avoid undesired workspace (i.e., singularity and joint limits) when given the actuation ability to follow the desired task space trajectory. This is investigated in this section by doing a *backward reachability* study.

4.1 Exoskeleton Control Task

As mentioned above, we are particularly interested in the four shoulder complex joints which are essential to realize
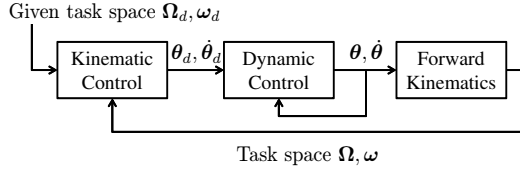
Fig. 6. Exoskeleton control structure.

3D orientation of the upper arm. Normally, the desired task is given in the task space (i.e., task space orientation $\boldsymbol{\Omega}_d$ and/or angular velocity $\boldsymbol{\omega}_d$ for the 4-DOF GH joint exoskeleton). To achieve the desired task, the following two control loops are typically utilized as shown in Fig. 6.

Kinematic Control   The first control loop is the kinematic control loop which generates the desired joint space trajectory (e.g., $\boldsymbol{\theta}_d$ and $\dot{\boldsymbol{\theta}}_d$) from the desired task space motion (e.g., $\boldsymbol{\Omega}_d$ and $\boldsymbol{\omega}_d$). A simple first-order inverse kinematic solution is given as (Bishop and Spong, 1998)

$$\dot{\boldsymbol{\theta}}_d = \boldsymbol{J}_o{}^{\dagger}(\boldsymbol{\omega}_d + \boldsymbol{K}_o \boldsymbol{e}_o) + (\boldsymbol{I} - \boldsymbol{J}_o{}^{\dagger}\boldsymbol{J}_o)\boldsymbol{\varphi}_N \qquad (8)$$

where $\boldsymbol{J}_o{}^{\dagger} = \boldsymbol{J}_o{}^T(\boldsymbol{J}_o\boldsymbol{J}_o{}^T)^{-1}$ is the *pseudo-inverse* of $\boldsymbol{J}_o$, $\boldsymbol{K}_o$ is a positive definite matrix, $(\boldsymbol{I} - \boldsymbol{J}_o{}^{\dagger}\boldsymbol{J}_o)$ is a projector into the null space of $\boldsymbol{J}_o$, and $\boldsymbol{\varphi}_N$ is an arbitrary vector to be designed. $\boldsymbol{e}_o$ is the task space *orientation error*, and the method to calculate $\boldsymbol{e}_o$ is well documented in Luh et al. (1980) and will not be detailed here. Note that, (8) provides infinite solutions due to the redundant exoskeleton design, whereas $\boldsymbol{\varphi}_N$ is the free variable to be designed to shape the final inverse kinematic solution to avoid reaching singularities and joint limits.

Dynamic Control   The dynamic control loop is used to control the exoskeleton joints to track the desired joint space trajectory. Since this study focuses on the kinematic control for singularity and joint limit avoidance, the dynamic control loop is simplified by assuming

$$\boldsymbol{\theta} = \boldsymbol{\theta}_d \qquad (9)$$

In reality, this simplification is reasonable since the dynamic control bandwidth is generally much higher than the kinematic control (Siciliano et al., 2009) and the animal-exoskeleton system normally does not require fast motions or rapid accelerations. This simplification will greatly reduce the computation complexity of the following reachability analysis (by reducing the state number of the continuous dynamics).

4.2 Backward Reachability Analysis

As discussed above, the overall question becomes that, given any task space motion, can we always find a proper $\boldsymbol{\varphi}_N$ to achieve the singularity and joint limit avoidance? With the help of MATLAB Level Set Toolbox (Mitchell and Templeton, 2005), this question can be answered by doing a *backward reachability* study (Lygeros et al., 1999; Tomlin et al., 2000). More specifically, we can define an unsafe set to represent the vicinity of singularity and joint limits, and then compute the backward time propagation from this unsafe set. The converged set is then the reachable set that may lead to the final unsafe set. This procedure is detailed as follows.

Continuous Dynamics   Due to the simplification of the dynamic control loop (i.e., $\boldsymbol{\theta} = \boldsymbol{\theta}_d$ and thus $\boldsymbol{e}_o = \boldsymbol{0}$), the continuous dynamics essentially reduces to the kinematic control equation (8) restated as

$$\dot{\boldsymbol{\theta}} = \boldsymbol{J}_o{}^{\dagger}(\boldsymbol{\theta})\boldsymbol{\omega}_d + \left[\boldsymbol{I} - \boldsymbol{J}_o{}^{\dagger}(\boldsymbol{\theta})\boldsymbol{J}_o(\boldsymbol{\theta})\right]\boldsymbol{\varphi}_N =: f(\boldsymbol{\theta}, \boldsymbol{u}, \boldsymbol{d}) \quad (10)$$

where $\boldsymbol{d} = \boldsymbol{\omega}_d \in \mathcal{D} \subset \mathbb{R}^3$ is the fictitious disturbance input trying to bring the system to the unsafe set, and $\boldsymbol{u} = \boldsymbol{\varphi}_N \in \mathcal{U} \subset \mathbb{R}^4$ is the control input to be designed to avoid the unsafe set. The corresponding input constraints are simply defined as hyper-rectangle, i.e., $\mathcal{D} = [-\boldsymbol{D}, \boldsymbol{D}]$ $(\boldsymbol{D} \succ \boldsymbol{0})$ and $\mathcal{U} = [-\boldsymbol{U}, \boldsymbol{U}]$ $(\boldsymbol{U} \succ \boldsymbol{0})$, where "$\succ$" means elementwise greater than.

Hamilton-Jacobi PDE   Let $J(\boldsymbol{\theta}, t): \mathbb{R}^n \to \mathbb{R}$ denote the *level function* $l(\boldsymbol{\theta})$ to be maximized by the control scheme over time, and $l(\boldsymbol{\theta})$ is a scalar function characterizing the "distance" from the unsafe region of the system. The optimal solution to this kind of problem can be referred to as a Stackelberg solution in a zero-sum dynamic game (Basar and Olsder, 1999; Tomlin et al., 2000). If $J(\boldsymbol{\theta}, t)$ is continuously differentiable, it satisfies the following Hamilton-Jacobi partial differential equation (PDE)

$$\frac{\partial J^*}{\partial t}(\boldsymbol{\theta}, t) + \min[0, H^*(\boldsymbol{\theta}, \boldsymbol{p})] = 0 \qquad (11)$$

$$J^*(\boldsymbol{\theta}, 0) = l(\boldsymbol{\theta}) \qquad (12)$$

where $\boldsymbol{p} = \frac{\partial J^*}{\partial \boldsymbol{\theta}}(\boldsymbol{\theta}, t)$, $l(\boldsymbol{\theta})$ is the level function to be designed later, and the optimal Hamiltonian is

$$
\begin{aligned}
H^*(\boldsymbol{\theta}, \boldsymbol{p}) &= \max_{\boldsymbol{u} \in \mathcal{U}} \min_{\boldsymbol{d} \in \mathcal{D}} H(\boldsymbol{\theta}, \boldsymbol{p}, \boldsymbol{u}, \boldsymbol{d}) \\
&= \max_{\boldsymbol{u} \in \mathcal{U}} \min_{\boldsymbol{d} \in \mathcal{D}} \boldsymbol{p}^{\mathrm{T}} f(\boldsymbol{\theta}, \boldsymbol{u}, \boldsymbol{d}) \\
&= \max_{\boldsymbol{u} \in \mathcal{U}} \min_{\boldsymbol{d} \in \mathcal{D}} \boldsymbol{p}^{\mathrm{T}} \left[\boldsymbol{J}_o{}^{\dagger}(\boldsymbol{\theta})\boldsymbol{d} + \left[\boldsymbol{I} - \boldsymbol{J}_o{}^{\dagger}(\boldsymbol{\theta})\boldsymbol{J}_o(\boldsymbol{\theta})\right]\boldsymbol{u}\right] \\
&= -\sum_{i=1}^{3} \left|\left[\boldsymbol{p}^{\mathrm{T}}\boldsymbol{J}_o{}^{\dagger}(\boldsymbol{\theta})\right]_i\right| \boldsymbol{D}_i \\
&\quad + \sum_{i=1}^{4} \left|\left[\boldsymbol{p}^{\mathrm{T}}\left(\boldsymbol{I} - \boldsymbol{J}_o{}^{\dagger}(\boldsymbol{\theta})\boldsymbol{J}_o(\boldsymbol{\theta})\right)\right]_i\right| \boldsymbol{U}_i \qquad (13)
\end{aligned}
$$

where $[\bullet]_i$ denotes the i-th entry of the vector $[\bullet]$. Note that, the control $\boldsymbol{u}$ and the disturbance $\boldsymbol{d}$ are decoupled from each other in the Hamiltonian. Thus, the maximization and the minimization can be conducted for each individual variable separately.

To compute the backward reachable set of the system state variables, the Level Set Toolbox also needs the upper bound of $\frac{\partial H^*}{\partial \boldsymbol{p}}$, which is essentially the upper bound of the optimal system state trajectory $\dot{\boldsymbol{\theta}}$ due to the optimality condition $\dot{\boldsymbol{\theta}} = \frac{\partial H^*}{\partial \boldsymbol{p}}$. By (10), the upper bound of the i-th entry of this gradient can be obtained as follows

$$
\begin{aligned}
\dot{\theta}_i(\boldsymbol{\theta}) &= \left[\boldsymbol{J}_o{}^{\dagger}(\boldsymbol{\theta})\boldsymbol{d}\right]_i + \left[\left(\boldsymbol{I} - \boldsymbol{J}_o{}^{\dagger}(\boldsymbol{\theta})\boldsymbol{J}_o(\boldsymbol{\theta})\right)\boldsymbol{u}\right]_i \\
&\leq \left|\left[\boldsymbol{J}_o{}^{\dagger}(\boldsymbol{\theta})\boldsymbol{d}\right]_i\right| + \left|\left[\left(\boldsymbol{I} - \boldsymbol{J}_o{}^{\dagger}(\boldsymbol{\theta})\boldsymbol{J}_o(\boldsymbol{\theta})\right)\boldsymbol{u}\right]_i\right| \\
&= \sum_{j=1}^{3} \left|\left[\boldsymbol{J}_o{}^{\dagger}(\boldsymbol{\theta})\right]_{ij}\right| \boldsymbol{D}_j + \sum_{j=1}^{4} \left|\left[\boldsymbol{I} - \boldsymbol{J}_o{}^{\dagger}(\boldsymbol{\theta})\boldsymbol{J}_o(\boldsymbol{\theta})\right]_{ij}\right| \boldsymbol{U}_j, \\
&\quad i = 1, 2, 3, 4. \qquad (14)
\end{aligned}
$$

where $[\bullet]_{ij}$ denotes the entry at the i-th row and the j-th column of the matrix $[\bullet]$.
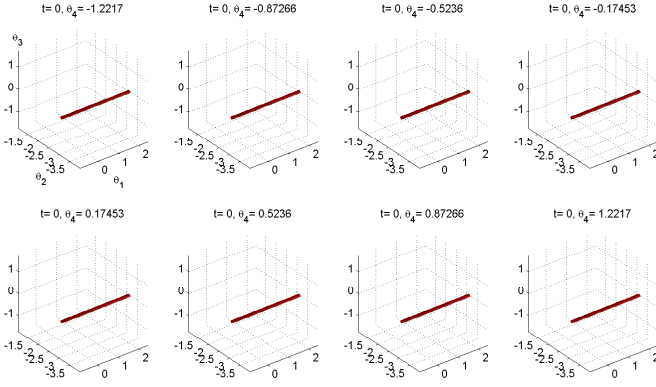
Fig. 7. Singularity unsafe set at t=0sec ($\theta_2 = -\pi$, $\theta_3 = 0$).

Level Function Design   Now we need to design proper level functions to characterize the unsafe set for reachability study. Recall that we have two issues in this kinematic control problem, i.e., the singularity and the joint limits. For singularity, the common metric used is the manipulability defined in (7). After normalization, the level function for singularity characterization is defined as $w_1 = \frac{c_m(\boldsymbol{\theta})}{c_m^{max}(\boldsymbol{\theta})} \in [0,1]$.

For the joint limit characterization, the metric can be defined as

$$c_l(\boldsymbol{\theta}) = 1 - e^{-k \prod\limits_{i=1}^{4} \frac{(\theta_i - \theta_{i\min})(\theta_{i\max} - \theta_i)}{(\theta_{i\max} - \theta_{i\min})^2}} \quad (15)$$

where $\theta_{i\min}$ and $\theta_{i\max}$ are the minimum and maximum position limits for the i-th joint as defined in Table 1, respectively. k is a scalar selected to make the maximum value of c_l at about 0.5. As expected, this c_l becomes smaller when θ_i approaches the corresponding joint limits. Similarly, the normalized metric is utilized as the level function to characterize the joint limit region, i.e., $w_2 = \frac{c_l(\boldsymbol{\theta})}{c_l^{max}(\boldsymbol{\theta})} \in [0,1]$.

In the following reachability study, we define the singularity unsafe set as $\sim 5^o$ from singular posture, which gives $w_1 \leq 0.0872$. Similarly, define the joint limit unsafe set as $\sim 2^o$ from one joint limit while the other joints are at their center points within the ranges, which gives $w_2 \leq 0.0553$. To avoid these two unsafe sets, the control objective becomes to maximize the time propagation of w_1 and w_2, i.e., $J(\boldsymbol{\theta}, t)$.

4.3 Unsafe Set Computing Results

The backward reachability study for the above problem formulation is coded using the Level Set Toolbox. The unsafe sets are propagated backward in time for 10sec, and the input bounds $\boldsymbol{U}$ and $\boldsymbol{D}$ are assigned based on the realistic motion speed and control signal parameters. In order to visualize the 4D unsafe set propagation, eight 3D slices along the fourth joint angle θ_4 are created and illustrated for each time instance (see Fig. 7 - Fig. 10). Another visualization issue is that, the joint limits are on the borders of the space (e.g., the unsafe set is outside the cube of each 3D space in Fig. 9 and Fig. 10). This makes the singularity unsafe set invisible inside the cube (safe set). To deal with this problem, the two unsafe sets are computed and visualized separately.
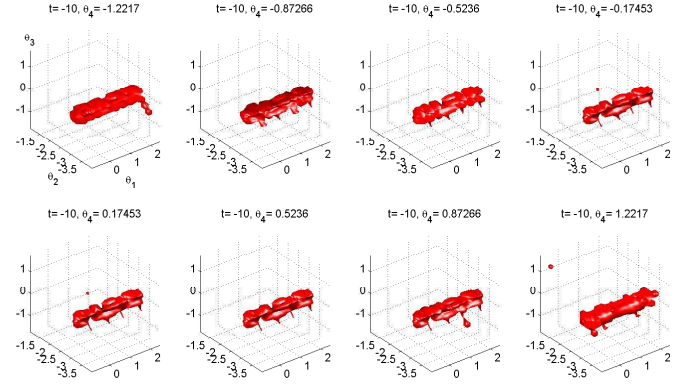
Fig. 8. Singularity unsafe set at t=−10sec.
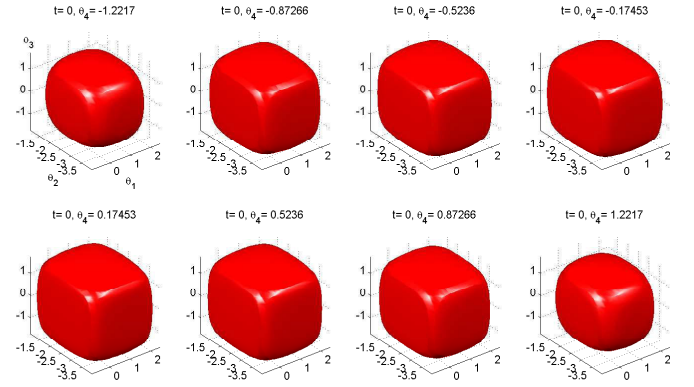
Fig. 9. Joint limit safe set at t=0sec.
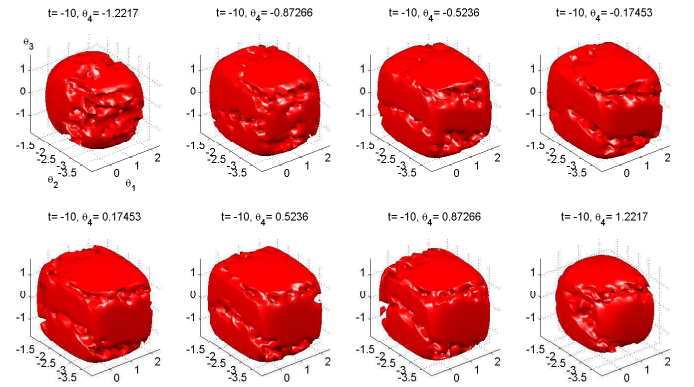
Fig. 10. Joint limit safe set at t=−10sec.

From Fig. 7 - Fig. 10, we can observe that both singularity unsafe set and joint limit unsafe set are expanding over time backward (i.e., red surfaces in Fig. 7 - Fig. 8 are expanding, and cubes in Fig. 9 - Fig. 10 are shrinking). Both unsafe sets converge to small invariant sets after finite time. This implies that the final safe region is still large, capable of achieving all 3D desired motion (this can be confirmed by doing a similar capture set computation). Thus, as long as we start from the safe region, there exists a feasible control to achieve the desired motion without reaching singularity or joint limits.

Recall that, in this problem, the disturbance $\boldsymbol{d}$ is the desired task space motion $\boldsymbol{\omega}_d$, which should be smooth and continuously differentiable in practice. For this reachability study, however, the disturbance is given too much advantage by allowing bang-bang disturbance which is

impossible in reality. As a result, the optimal Hamiltonian is underestimated and the unsafe set is overestimated, i.e., in practice it is more unlikely to reach the extreme unsafe sets computed here. With this reachability study, it is confirmed that the feasible solution to avoid reaching singularity and joint limits exists with the control variable $\boldsymbol{u}_s$. This will provide a guidance for designing a practical kinematic controller based on these level functions to achieve the desired objectives.

5. CONCLUSION

A 6-DOF macaque upper limb exoskeleton model with 4 DOFs at the shoulder complex was proposed for a BMI study in this paper. With one redundant DOF assigned to the shoulder complex, the kinematic analysis and the backward reachability analysis study demonstrated the feasibility for the proposed model to avoid both the singularity and the joint limits. The non-motorized version of the proposed model has been built. As an immediate future work, the macaque motion data acquisition and system calibration will be conducted to experimentally verify the feasibility of the proposed upper limb exoskeleton design.

ACKNOWLEDGEMENTS

REFERENCES

Ball, S., Brown, I., and Scott, S. (2007). MEDARM: a rehabilitation robot with 5DOF at the shoulder complex. In *Proc. IEEE/ASME Int. Conf. on Adv. Intell. Mech. (AIM)*, 1–6.

Basar, T. and Olsder, G.J. (1999). *Dynamic Noncooperative Game Theory*. SIAM Classics, 2nd edition.

Bishop, B.E. and Spong, M.W. (1998). Control of redundant manipulators using logic-based switching. In *Proceedings of the 37th IEEE Conference on Decision and Control*, volume 2, 1488–1493.

Bowker, J.H. (1992). *Atlas of limb prosthetics: surgical, prosthetic, and rehabilitation principles*. Mosby-Year Book.

Christopher & Dana Reeve Foundation, L. (2009). One degree of separation - paralysis and spinal cord injury in the united states. Technical report, Christopher & Dana Reeve Foundation.

Cott, H.P.V. and Kinkade, R.G. (1972). *Human Engineering Guide to Equipment Design*. McGraw-Hill, Washington D. C., U.S.A., revised edition.

Ergin, M.A. and Patoglu, V. (2012). ASSISTON-SE: A self-aligning shoulder-elbow exoskeleton. In *IEEE Int. Conf. on Robotics and Automation (ICRA)*, 2479–2485.

Johnson, G., Carus, D., Parrini, G., Marchese, S.S., and Valeggi, R. (2001). The design of a five-degree-of-freedom powered orthosis for the upper limb. In *Proc Inst Mech Eng H.*, volume 215, 275–284.

Kim, J.O. and Khosla, P.K. (1991). Dexterity measures for design and control of manipulators. In *IEEE/RSJ International Workshop on Intelligent Robots and Systems (IROS)*, volume 2, 758–763.

Letier, P., Avraam, M., Veillerette, S., Horodinca, M., Bartolomei, M.D., Schiele, A., and Preumont, A. (2008). SAM: A 7-DOF portable arm exoskeleton with local joint control. In *IEEE/RSJ Int. Conf. on Intelligent Robots and Systems (IROS)*.

Luh, J.Y.S., Walker, M.W., and Paul, R.P.C. (1980). Resolved-acceleration control of mechanical manipulators. *IEEE Trans. Automat. Contr.*, AC-25(3), 468–474.

Lygeros, J., Tomlin, C., and Sastry, S. (1999). Controllers for reachability specifications for hybrid systems. *Automatica*, 35, 349–370.

Martinez, F., Retolaza, I., Pujana-Arrese, A., Cenitagoya, A., Basurko, J., and Landaluze, J. (2008). Design of a five actuated dof upper limb exoskeleton oriented to workplace help. In *2nd IEEE/RAS-EMBS Int. Conf. on Biomedical Robotics and Biomechatronics (BioRob)*, 169–174.

Mihelj, M., Nef, T., and Riener, R. (2006). ARMin - Toward a six DoF upper limb rehabilitation robot. In *The First IEEE/RAS-EMBS Int. Conf. on Biomedical Robotics and Biomechatronics (BioRob)*, 1154–1159.

Mihelj, M., Nef, T., and Riener, R. (2007). ARMin II - 7 DoF rehabilitation robot: mechanics and kinematics. In *IEEE Int. Conf. on Robotics and Automation (ICRA)*, 4120–4125.

Mitchell, I.M. and Templeton, J.A. (2005). A toolbox of Hamilton-Jacobi solvers for analysis of nondeterministic continuous and hybrid systems. In *Hybrid Systems Computation and Control*, volume 3414, 480–494. Springer, Heidelberg.

Nef, T. and Riener, R. (2008). Shoulder actuation mechanisms for arm rehabilitation exoskeletons. In *2nd IEEE/RAS-EMBS Int. Conf. on Biomedical Robotics and Biomechatronics (BioRob)*, 862–868.

Peat, M. (1986). Functional anatomy of the shoulder complex. *Phys Ther*, 66(12), 1855–1865.

Perry, J., Rosen, J., and Burns, S. (2007). Upper-limb powered exoskeleton design. *IEEE/ASME Trans. Mechatronics*, 12(4), 408–417.

Romilly, D.P., Anglin, C., Gosine, R.G., Hershler, C., and Raschke, S.U. (1994). A functional task analysis and motion simulation for the development of a powered upper-limb orthosis. *IEEE Trans. Rehabil. Eng.*, 2(3), 119–129.

Siciliano, B., Sciavicco, L., Villani, L., and Oriolo, G. (2009). *Robotics: Modelling, Planning and Control*. Springer, 2nd edition.

Tomlin, C., Lygeros, J., and Sastry, S. (2000). A game theoretic approach to controller design for hybrid systems. *Proceedings of the IEEE*, 88, 949–970.

Tsagarakis, N.G. and Caldwell, D.G. (2003). Development and control of a 'soft-actuated' exoskeleton for use in physiotherapy and training. *Journal of Autonomous Robots*, 15(1), 21–33.

Yang, J., Abdel-Malek, K., and Nebel, K. (2005). Reach envelope of a 9-degree-of freedom model of the upper extremity. *International Journal of Robotics & Automation*, 20(4), 240–259.

Yoshikawa, T. (1985). Manipulability of robotic mechanisms. *The International Journal of Robotics Research*, 4(2), 3–9.